Alzheimer's pathology disrupts flexible place cell coding and hippocampal-prefrontal neural dynamics during risky foraging decisions in mice

Eun Joo Kim[1*], Sanggeon Park[2], Bryan P. Schuessler[1], Harry Boo[1], Jeiwon Cho[2*], and Jeansok J. Kim[1,3*]

[1]Department of Psychology, University of Washington, Seattle, WA 98195-1525, USA

[2]Department of Brain and Cognitive Sciences, Scranton College, Ewha Womans University, Seoul, 03760, Republic of Korea

[3]Neuroscience Program, University of Washington, Seattle, WA 98195-1525, USA

***Correspondence:**

Eun Joo Kim, Department of Psychology, University of Washington, Seattle, WA 98195, USA. E-mail: ejkim731@u.washington.edu

Jeiwon Cho, Department of Brain and Cognitive Sciences, Scranton College, Ewha Womans University, Seoul, 03760, Republic of Korea. E-mail: jelectro21@ewha.ac.kr

Jeansok J. Kim, Department of Psychology, University of Washington, Seattle, WA 98195, USA. E-mail: jeansokk@u.washington.edu

SUMMARY

This study investigates the neural activity patterns associated with impaired decision-making in Alzheimer's disease (AD) by examining the effects of amyloid pathology on prefrontal-hippocampal circuit dynamics in 5XFAD mice, a model system known for its pronounced early amyloid pathology. Using ecologically relevant “approach food-avoid predator” paradigms, we revealed that 5XFAD mice display impaired decision strategies in risky foraging tasks, characterized by rigid hippocampal place fields and diminished sharp-wave ripple (SWR) frequencies, accompanied by disrupted prefrontal-hippocampal connectivity. These neural deficits align with behavioral inflexibility in dynamic threat scenarios. Our findings indicate that disrupted SWR dynamics and corticolimbic connectivity contribute to decision-making deficits in AD, emphasizing the potential of targeting these specific neural mechanisms to ameliorate cognitive impairments. This research contributes significantly to our understanding of AD's impact on cognition, providing insights that could lead to more targeted therapeutic strategies.

KEYWORDS

Alzheimer’s disease, risky decision-making; 5XFAD mouse; hippocampus; medial prefrontal cortex; simultaneous recording; spike synchrony; predatory threat; behavioral flexibility

INTRODUCTION

The natural process of aging is the leading risk factor for Alzheimer's disease (AD), a prevalent form of dementia that profoundly impacts the quality of human life and increases healthcare costs in today's increasingly long-living society. Preclinical research has closely linked physical brain changes in AD to memory impairments; however, other cognitive functions such as decision-making are also adversely affected [1,2]. Studies have shown that AD impairs decision-making, particularly regarding the uncertainty of financial risks involving rewards and losses [3-6]. Despite the crucial importance of decision-making in daily life, research on this aspect of AD, especially in animal models, remains sparse [7-9]. Furthermore, while numerous studies have identified structural brain anomalies like amyloid plaques and neurofibrillary tangles through postmortem analyses of human and animal model AD brains, there has been little effort to understand the neural computational disruptions that occur in living AD brains during behavior. Hence, there is a crucial need to explore the neurocircuit mechanisms that contribute to AD's detrimental effects on decision-making processes.

Research indicates the vital role of the medial prefrontal cortex (mPFC) and its interactions with limbic areas, such as the dorsal hippocampus (dHPC), in decision-making. Damage or inactivation of these regions disrupts risk-based decisions in rodents, monkeys, and humans [10-15]. Specifically, functional magnetic resonance imaging (fMRI) studies in humans subjected to probabilistic monetary gains/losses, and single-unit recording studies in animals engaged in probabilistic/delay discounting of dietary rewards, have linked risky decision-making to neural activity in the mPFC and dHPC [12,16]. Recent findings indicate that AD patients struggle with decision-making

under financial uncertainty scenarios [6] and face challenges in set-shifting tasks [9], likely due to accumulations of Aβ plaques and tau neurofibrillary tangles in the dHPC and mPFC. However, the exploration of risky decision-making in ecologically-relevant settings and the simultaneous characterization of neuronal activity in the mPFC and dHPC during the early, clinically-relevant phase of AD have not been thoroughly explored.

Our recent work has documented ensemble neural activities in rats during goal-directed foraging in a realistic risky environment [17,18]. Our findings revealed that dHPC place cells encode spatial-danger gradients, while mPFC cells anticipate food procurement and predatory threats. Notably, place cells near a dynamic predatory robot exhibit unstable firing patterns, contrasting with the stable firing observed in safer areas, such as inside and near the nest. Furthermore, a subset of mPFC neurons increased their activity when animals cautiously approach a stationary predator, indicating the mPFC's role in risk assessment and decision-making. These observations suggest the potential utility of ecologically-relevant risky foraging paradigms for investigating alterations in decision-making processes in AD [5,7,9] and abnormal neuronal activities in the mPFC and dHPC across various AD mouse models.

This study utilizes the 5XFAD transgenic mouse model, known for its pronounced amyloid pathology from an early (3 months) age due to overexpression of amyloid precursor protein (APP) and presenilin 1 (PS1) [19-22]. We focus on dHPC sharp-wave ripples (SWRs) and mPFC-dHPC connectivity. SWRs are brief, high-frequency (150-250 Hz) oscillations linked to decision-making and emotional responses [23,24], and

they interact with mPFC activity during cognitive tasks [25-27]. Notably, reductions in SWRs, observed in both APP/PS1 [28] and 5XFAD [29] mice, are linked to deficits in hippocampal inhibitory synaptic connections [30] and reflect early SWR deficits in apolipoprotein E4 knockin (ApoE4-KI) mice. The latter models the human ApoE4 allele, a major genetic risk factor for AD that influences Aβ metabolism, aggregation, and deposition, and these deficits correlate with subsequent spatial memory impairments [31,32]. By leveraging the premise that naturalistic environments with dynamic elements can profoundly influence, modulate, or reshape neural processes and behavioral outcomes [33-36], we adapted the 'approach food-avoid predator' conflict paradigm, originally developed for rats [37,38], to our mouse model. This adaptation allows for a broader exploration of AD's impact on cognition and neural activity in the dHPC and mPFC, providing insights into the neural dynamics and behavioral patterns associated with risky decision-making in AD.

RESULTS

5XFAD mice exhibit risk-prone foraging in an escalating predatory task

During baseline foraging, both 5XFAD and WT groups readily left the nest and procured pellets comparably (Figure S1A). The day after the last baseline assessment, animals underwent a weasel predator test (Figure 1A). Data from different sex and age groups were pooled due to the absence of significant differences (Figures S1B and S1C). On the first day of predator testing, both groups initially fled into the nest in response to the surging weasel, exhibiting a significantly increased latency in procuring pellets at 38.1 cm compared to baseline (Figure 1B). At the 25.5 cm pellet distance,

while WT mice continued to display risk-averse foraging, 5XFAD mice demonstrated risk-prone foraging. At the shortest distance of 12.7 cm, both groups successfully obtained the pellet, with WT and 5XFAD mice showing similar and shorter latencies compared to their baseline levels, respectively. Overall, 5XFAD mice exhibited a shorter mean latency across trials compared to WT mice (Figure 1C). Across all three distances, there were no significant group differences in running speed (velocity), latency to enter foraging area (except for 25.4 cm distance), and number of attempts at pellets (Figures 1D, S2A, and S2B). The second day of testing mirrored these patterns, with no significant differences in overall latency between groups observed (Figures S2C and S2D). Aβ staining and histological analysis revealed higher levels of plaque deposits in the dCA1 and mPFC in 5XFAD mice compared to WT mice (Figures 1E-1G). These findings suggest that Aβ accumulation in 5XFAD mice may alter their ability to discern safety boundaries under predatory threat, yet does not affect their predator-responsiveness or pellet motivation levels.

5XFAD mice exhibit inflexible foraging and rigid place cell coding in a conditional predatory task

When the preferred pellet arm was rendered dangerous by pairing the animal's approach with a looming predator (Figures 2A and 2B), WT mice readily switched foraging to the non-preferred pellet arm, which was not coupled with a predatory threat (Figure 2C). In contrast, 5XFAD mice showed a persistent propensity to continue visiting the predator-associated preferred pellet arm, as indicated by

significantly higher preference index (PI) values than WT mice (Figure 2D). Despite 5XFAD mice maintaining preferred (risky) arm or WT mice shifting to non-preferred (safe) arm, both groups displayed a decrease in movement speed during the predator session compared to the pre-predator session, reflecting their hesitancy to approach the pellet in the presence of the robot. However, there were no significant differences in overall movement speed between the groups during the pre-predator and predator sessions (Figure 2E). Aβ deposit levels in the dHPC and mPFC of 5XFAD mice subjected to the conditional predatory task were higher compared to WT levels (Figures 2F and 2G). These results, showing continued preference for dangerous pellets in 5XFAD mice, indicate a deficit in adaptive behavioral switching in response to perceived danger in AD.

Building on previous findings of place cell behavior in rats under predatory threats [18,41], we analyzed place cell activity in 5XFAD mice to assess the impact of amyloid pathology on threat distance-dependent place cell remapping (Figure 2H). We collected dHPC place cell data from 6 WT (94 units) and 11 5XFAD (112 units) mice, categorizing cells based on their maximal firing location during the pre-predator session (Figures 2I, S3A, and S3B): nest cells (WT, n = 22; 5XFAD, n = 35), center-arm cells (WT, n = 27; 5XFAD, n = 29), risky-arm cells (WT, n = 20; 5XFAD, n = 22), and safe-arm cells (WT, n = 15; 5XFAD, n = 8). WT mice exhibited lower pixel-by-pixel correlation (Z') in risky-arm and center-arm cells compared to nest cells, indicating place cell remapping in riskier areas (Figure 2J). Correspondingly, WT risky-arm cells also showed increased peak distance compared to the nest cells (Figure 2K). However, 5XFAD place cells did not demonstrate place field remapping across maze zones as measured by both spatial

correlation and peak distance, suggesting impaired spatial-fear representation (Figures 2J and 2K). While there was a group difference in place field size of risky-arm cells during the pre-predator session, the field size was not correlated with spatial correlation or peak distance between the sessions (Figures S3B-S3D). This suggests that the changes in spatial correlations in 5XFAD risky-arm cells cannot be fully attributed to differences in place field size. The WT place fields in the safe-arm, in contrast to those in the risky-arm, showed levels of spatial correlation and peak distance similar to those of nest place fields (Figure S4A and S4B). Since 5XFAD mice rarely visited the nonpreferred arm during both pre-predator and predator sessions, no further analysis was conducted on safer-arm place cells. These data suggest that in dynamic dangerous environments, dHPC place fields in 5XFAD mice remained rigid, lacking the threat location-specific remapping observed in WT mice.

5XFAD mice exhibit alterations in SWRs and associated activity changes in dHPC during risky decision-making

We analyzed SWRs in the dHPC and their interaction with dHPC neuronal firings across sessions. Both WT and 5XFAD mice exhibited SWR activity (Figure 3A), but 5XFAD mice had reduced dCA1 SWRs compared to WT mice throughout the sessions (Figure 3B, Left). The duration of SWRs was comparable between the two groups during the pre-predator session, while the 5XFAD mice showed shorter SWRs compared to the WT mice during the predator session (Figure 3B, Right). We further explored the peri-SWR activity (within a $\pm$250 ms period around SWR peak timing) in the dHPC during pre-predator and predator sessions (Figure 3C).

Comparable proportions of dHPC units exhibited significant (z > 3) peri-SWR firing during the predator session in both groups (dHPC: 49.7% for WT, 53.3% for 5XFAD; mPFC: 27.8% for WT, 32.8% for 5XFAD). The mean firing rates during a ±250 and ±100 ms periods of these cells in both groups were higher than the pre-predator levels (Figures 3D and 3E). However, while the majority of the SWR-associated dHPC cells in WT exhibited peak firing closely aligned with SWR events (Figure 3F), those in 5XFAD animals showed their maximal firing rates at significantly longer time lags relative to SWR events (Figure S5A). The peak firings of WT dHPC cells during the ±250 ms and ±100 ms periods were significantly higher than those of the 5XFAD dHPC cells (Figure 3G). These results indicate disrupted temporal dynamics between dHPC SWRs and hippocampal cells in 5XFAD compared to WT dHPC cells.

Additionally, we analyzed SWRs in the dHPC and their interaction with dHPC neuronal firings during rest immediately after predator encounters (Figure S5B). During this post-predator recording session in nest, 5XFAD mice continued to show fewer and shorter dCA1 SWRs compared to WT mice (Figure S5C), with no significant group difference in movement speed (Figure S5D). The peri-SWR activity (within a ±250 ms period around SWR peak timing) in the dHPC during the post-predator session (Figure S5E) demonstrated a higher proportion of SWR-modulated dHPC activity with shorter time lags in WT compared to 5XFAD mice (Figure S5F) as well as a farther peak timing from SWR onset (Figure S5G). Additionally, the maximal firing of the WT dHPC cells during the ±250 ms was significantly higher compared to that of 5XFAD dHPC cells (Figure S5H). These results suggest that amyloid pathology may affect SWR activity and SWR-associated cell firing patterns in dHPC while animals process predator-

associated foraging information immediately after predator encounters. Lastly, we explored the relationship between amyloid load, SWR activity, and behavioral flexibility. The amyloid plaques in dHPC and mPFC were correlated with both behavioral switch (i.e., the PI values; Figure S6A) and the SWR frequency throughout the sessions (Figure S6B), and SWR frequency was also correlated with PI values (Figure S6C). These significant correlations suggest a link between Aβ deposition, SWR activity levels, and adaptive behavior under threat. Taken together, these findings indicate that SWR-associated hippocampal network activity could serve as *in vivo* biomarkers for AD, potentially leading to impairments in risky decision-making.

5XFAD mice exhibit alterations in dynamics in dHPC-mPFC interactions during risky decision-making

Next, we analyzed SWRs in the dHPC and their interaction with mPFC neuronal firings across sessions (Figure 4A). Similar proportions of mPFC units exhibited significant ($z > 3$) peri-SWR firing during the predator session in both groups (38.3% for WT, 31.9% for 5XFAD). The mean firing rates during a $\pm$500 and $\pm$250 ms periods of these cells in WT mice were higher than pre-predator levels (Figure 4B). However, predator-induced SWR modulation was not observed in 5XFAD, showing no significant difference in mean relative firing rates in mPFC relative to dHPC SWR onset between sessions (Figure 4C). While the ratio of the mPFC cells peaking closely aligned with SWR events did not differ between WT and 5XFAD mice (Figure 4D), the mPFC cells peaking at $\pm$250 from the SWR onset showed higher peak Z

values compared to those of 5XFAD mPFC cells (Figure 4E). We then examined dHPC and mPFC cell interactions in the center (decision) zone before animals turned toward preferred (risky) arm or non-preferred (safe) arm (Figure 4F). Cross-correlograms (CCs) with mPFC cells as the reference were generated during pre-predator and predator decision points (3-s epoch before turns). A total of 1,060 dHPC-mPFC neuronal pairs (462 pairs in WT and 598 pairs in 5XFAD) were recorded throughout the sessions. Out of these, 222 pairs in WT and 251 pairs in 5XFAD mice, which exhibited average firing rates greater than 0.2 Hz, were subsequently selected for further analysis. A higher proportion of WT pairs (45 pairs, 20.3%) showed significant synchrony at the predator decision point than 5XFAD pairs (26 pairs, 10.4%), indicating reduced dHPC-mPFC spike synchrony in 5XFAD mice (Figure 4G). The mean and peak dHPC firing rates during a $\pm$100 ms period following mPFC spikes in both groups were higher than pre-predator levels (Figures 4H and 4I). Taken together, these results suggest that 5XFAD mice exhibit reduced predator-induced modulation of dHPC SWR-associated mPFC cell firing patterns and decreased dHPC-mPFC spike synchrony under predatory threat.

After completing the conditional predatory task, mice underwent contextual fear conditioning for 2 days (Figure 4J). 5XFAD and WT mice exhibited similar levels of contextual fear conditioning, demonstrated by equivalent postshock freezing on both days 1 and 2, as well as contextual freezing on day 2 (Figures 4K, 4L, S7A, and S7B). These findings suggest that 5XFAD mice have normal responses to footshocks and learned fear behavior. Therefore, the observed alterations in risky foraging decision-making in 5XFAD mice are not likely due to general changes in response to aversive stimuli and learning.

DISCUSSION

This study, utilizing two distinct predatory scenarios and simultaneous mPFC-dHPC recordings in the 5XFAD mouse model, provides new insights into the behavioral patterns and neural dynamics associated with risky decision-making in AD. Behaviorally, 5XFAD mice exhibited risky tendencies, such as traveling longer distances for foraging and displaying inflexible strategies, despite demonstrating normal contextual fear conditioning and reliably fleeing from closely approaching predatory agents, compared to WT counterparts. This observation highlights a critical aspect of amyloid pathology affecting decision-making under risk, reflecting cognitive impairments faced by AD patients [5,6,46,47]. The aberration in risky decision-making was consistently observed in both 4-5 and 7-8 month-old 5XFAD mice, suggesting that our ecologically relevant risky decision-making paradigms could serve as potential early diagnostic tools for AD.

The increased risky decision-making in 5XFAD mice is accompanied by alterations in dCA1 SWRs and distinct mPFC-dHPC neural dynamics. The reduction in the frequency and duration of dCA1 SWRs in 5XFAD mice is significant, as SWRs are proposed as a “cognitive biomarker” [48] of various cognitive processes, including memory consolidation, retrieval, and planning [48-50]. In support, real-time disruptions and elongations of hippocampal SWRs have been shown to impair and improve working memory, respectively [27,51]. Furthermore, SWRs decrease with aging [52,53] and in AD mouse models [28,29]. The present study’s finding of correlations between Aβ plaques, SWR activity and behavioral patterns suggests that impaired hippocampal SWR activity could be a key factor behind the decision-making deficits

in 5XFAD mice. This finding aligns with previous research emphasizing the significance of SWRs in spatial memory and navigation, which are closely related to decision-making under risk [25,48-51,54].

While the proportion of dHPC cells that significantly fired during predator encounters was comparable between 5XFAD and WT animals, 5XFAD hippocampal cells demonstrated a greater deviation in their firing time relative to the peak of SWR compared to WT dHPC cells. This indicates reduced synchronous activity between SWR events and hippocampal cells, aligning with previous findings of weaker coactivation among hippocampal cell pairs during SWR events [30]. Such deviation may contribute to incoherent hippocampal cell activity with SWRs in 5XFAD mice. Additionally, given that the SWR-associated activity of mPFC cells supports rule switching, adaptive action selection, and accurate memory-guided performance [26,55,56], the deficits in the timely coordination between mPFC neurons and dHPC SWRs under conditional threat situations may be linked to the decreased behavioral flexibility observed in 5XFAD mice. This observation suggests that enhancing SWR activity or hippocampal-mPFC connectivity, potentially through lifestyle interventions such as exercise and diet [57,58], as well as pharmacological [59], genetic [60], neuromodulation [61], or gut microbiome [62] approaches, might be effective strategies for delaying and alleviating decision-making deficits in AD.

Previous studies utilizing Aβ mouse models have revealed amyloid pathology-induced alterations in the coding properties of place cells, although results have been variable. For instance, 16-month-old Tg2576 mice exhibited reduced spatial information and enlarged place field size [63], while 4-14-month-old 5XFAD mice demonstrated the

opposite effects [64]. Furthermore, place field stability varied across AD mouse models. The 3xTg mouse model, which develops both Aβ and tau pathologies in an age-dependent manner, showed less stable place fields in a circular maze compared to control animals at 8-9 months [65]. In contrast, studies have reported stable place firing in familiar contexts for 7-13-month-old APP KI and 7-month-old J20 APP mice [66,67]. Notably, Aβ animals displayed deficits in the experience-dependent flexibility of spatial coding; APP-PS1 place cells failed to adapt to learning-induced changes in their firing patterns [68]. Interestingly, while APP KI mice maintained stable spatial representations on a familiar linear track, they were impaired in developing remapping when introduced to a different linear track [66]. Our findings of rigid place firing in 5XFAD mice in areas associated with predatory threats indicate an impairment in the ability to encode changes in spatial-danger information. This adds a spatial dimension to the decision-making deficits observed in AD, highlighting a vulnerability in integrating spatial and risk information due to AD pathology. These observations align with the existing literature on spatial memory impairments in AD [69-71], suggesting that these deficits may also extend to spatially informed decision-making processes.

A few caveats must be considered when interpreting the findings of this study. First, while 5XFAD mice demonstrated unimpaired contextual fear learning (postshock freezing) and memory (retention tests), which are believed to engage the hippocampus [72,73], this does not exclude the possibility that reduced innate fear in 5XFAD mice contributed to the present study's outcomes. Additionally, an earlier study [74] found normal contextual fear in younger 5XFAD mice (i.e., < 4 months) and

impaired contextual fear in older 5XFAD mice (i.e., 6 months). In our study, however, analysis of contextual freezing data revealed no genotype difference, despite the mice being 8-11 month old at the time of fear conditioning. This finding is consistent with another study where APP-KI mice aged 12-13 months exhibited similar levels of contextual freezing as their WT counterparts [66]. Second, the alterations in decision-making behaviors observed in our study may involve Aβ pathology beyond the hippocampal-mPFC circuit. Future studies are needed to determine whether amygdalar neurons in different subnuclei respond differently to predatory-evoked innate fear versus pain-associated learned fear, as well as age-dependent changes.

In summary, our research underscores the importance of using ecologically-relevant tasks to uncover the intricate nature of cognitive deficits in AD. By simulating real-life decision-making scenarios under risk, we gain a more nuanced understanding of AD pathology than is possible with traditional behavioral tasks. Importantly, the reliable detection of behavioral and neural alterations in 5XFAD mice with Aβ accumulations—without tau pathology—suggests that an ecological screening approach could facilitate earlier detection of AD and the development of targeted therapeutic interventions. Specifically, future research should explore the potential of enhancing SWR activity and hippocampal-mPFC connectivity as means to prevent cognitive decline and restore cognitive function in AD.

FIGURE LEGENDS

FIGURE 1. 5XFAD mice exhibit risk-prone foraging in an escalating predatory task (A) Image of a foraging mouse facing a predatory weasel and the associated behavioral procedure. (B) Latency to procure pellets in WT (n = 17) and 5XFAD (n = 17) mice during weasel testing (Friedman test and Wilcoxon signed-rank test). (C) Mean latency to procure pellets across the three weasel trials in WT and 5XFAD mice (*t*-test). (D) The left three columns show approach (prior to weasel activation) and escape (subsequent to weasel activation) velocity in WT and 5XFAD mice at distances of 38.1 cm, 25.4 cm, and 12.7 cm. The rightmost column illustrates that there were no group differeneces in approach-escape speed across the three distance trials (around −500 and 500 ms from weasel, *t*-test). (E) Representative photographs showing Aβ plaque buildup in the dCA1 and mPFC from a 5XFAD mouse but not in a WT mouse. (F,G) Mean area percentage of Aβ accumulation in dCA1 (G) and mPFC (H) of WT and 5XFAD mice (Mann–Whitney *U* test). Data are represented as mean ± SEM. $^{**}P < 0.01$, $^{***}P < 0.001$, $^{****}P < 0.0001$.

FIGURE 2. 5XFAD mice exhibit inflexible foraging and rigid place cell coding in a conditional predatory task (A) Image of a mouse tethered for neural recording in the T-maze apparatus. (B) Depiction of the behavioral procedure consisting of successive pre-predator (without predator) and predator (with predator) sessions. (C) Comparison of successful procurement of preferred (P) and non-preferred (NP) pellets between the pre-predator and predator sessions in WT and 5XFAD mice (Wilcoxon signed-rank test). (D) Preference index (ratio of preferred pellet choices to total choices) during the

predator session in WT and 5XFAD mice (Mann-Whitney *U* test). (E) The overall speed during the pre-predator and predator sessions (Two-way repeated measures ANOVA). (F,G) Mean area percentage of Aβ accumulation in dCA1 (F) and mPFC (G) of WT and 5XFAD mice (*t*-test). (H) Tetrode recordings of dHPC place cells (*Top*) and the designated zones in the T-maze (*Bottom*): Nest, Center zone, Risky arm and Safe arm. (I) Examples of wave forms and place fields from the nest, center, and risky arm cells during the pre-predator and predator sessions in WT (*Left*) and 5XFAD (*Right*) mice. The color scale (red, maximal firing; blue, nospike) corresponds to the firing rate for each unit. The numerical value represents the peak firing rate for each session. (J,K) Spatial correlations (J) and peak distances (K) between pre-predator and predator sessions within the nest, center, and risky arm (Bonferroni test and Mann-Whitney *U* test). Data are represented as mean ± SEM. *$P < 0.05$, **$P < 0.01$, ***$P < 0.001$, ****$P < 0.0001$.

FIGURE 3. 5XFAD mice exhibit alterations in SWRs and associated activity changes in dHPC during risky decision-making (A) Tetrode recordings of dHPC SWR activities. LFP signals were filtered (150-250 Hz) for SWR analysis. (B) Mean frequency (*Left*) and duration (*Right*) of SWRs in WT and 5XFAD mice across sessions. (C) dHPC SWR and unit activities were analyzed during the pre-predator and predator sessions, highlighting color-coded dHPC unit activity (significant Z scores) during peri-SWR epochs, aligned with SWR onset in each session. (D,E) Peri-SWR activity (mean Z-scores) of WT (D) and 5XFAD (E) dHPC neurons showing significant activity ($z > 3$) within the ±250 ms (blue) and ±100 ms (orange) periods around SWR onset during the

predator session. Mean Z-scores were compared bewteen sessions (Wilcoxon signed-rank test). (F) Proportions of dHPC neurons exhibiting significant activity within the ±250 ms vs. ±100 ms periods were compared between the WT and 5XFAD groups (Chi-square test). (G) SWR-related dHPC cell activity (peak Z-scores within the ±250 ms and ±100 ms periods) during the predator session in WT and 5XFAD mice (Mann-Whitney *U* test). Data are represented as mean ± SEM. *$P < 0.05$, **$P < 0.01$, ***$P < 0.001$.

FIGURE 4. 5XFAD mice exhibit alterations in dynamics in dHPC-mPFC interactions during risky decision-making (A) dHPC SWR and unit activities were analyzed during the pre-predator and predator sessions, highlighting color-coded mPFC unit activity (significant Z scores) during peri-SWR epochs, aligned with SWR onset in each session. (B) Peri-SWR activity (mean Z-scores) of WT mPFC neurons exhibiting significant activity ($z > 3$) within the ±500 ms (blue) and ±250 ms (orange) periods around SWR onset during the predator session. Mean Z-scores were compared between sessions (paired *t*-test). (C) Peri-SWR activity (mean Z-scores) of 5XFAD mPFC neurons showing significant activity ($z > 3$) within the ±250 ms (blue) and ±100 ms (orange) periods around SWR onset during the predator session. Mean Z-scores during the ±500 ms and ±250 ms windows were compared between sessions (Wilcoxon signed-rank test and paired *t*-test). (D) Proportions of mPFC neurons exhibiting significant activity within the ±250 ms vs. ±100 ms periods in the WT and 5XFAD groups (Chi-square test). (E) SWR-related mPFC cell activity (peak Z-scores) during the predator session in WT and 5XFAD mice (Mann-Whitney *U* test and *t*-test). (F) Analysis of synchronous activity between dHPC and mPFC units during pre-predator and

predator sessions. Color-coded CCs indicate significant cell pairs with increased dHPC-mPFC spike synchrony during the 3-s epochs before the animals made turns (pre-turn) in the presence of the predator. (G) Of the available CCs, 20.3% of WT (*Left*) and 10.4% of 5XFAD (*Middle*) CCs showed significant correlated firing during the predator session. The proportion of the significant dHPC-mPFC CCs in WT and (Chi-square test). (H,I) Averaged dHPC-mPFC CCs from WT (H) and 5XFAD (I) mice showing significant peaks (between −100 and 100 ms; blue area) during pre-turn epochs in the presence of the predator (*Left*). Mean (*Middle*) and peak (*Right*) Z scores within the ±100 ms period during the pre-predator and predator sessions in WT and 5XFAD mice (paired *t*-test and Wilcoxon signed-rank test). Shaded areas indicate SEM. (J) Behavioral procedure for contextual fear conditioning. (K,L) Levels of freezing during the pre-shock (3 min) and post-shock (3 min) phases On days 1 (K) and 2 (L) (*t*-test). Data are represented as mean ± SEM. *$P < 0.05$, **$P < 0.01$, ***$P < 0.001$, ****$P < 0.0001$.

METHOD DETAILS

Animals

5XFAD transgenic mice, overexpressing amyloid precursor protein and presenilin 1, along with their littermate WT mice counterparts (aged 4-8 weeks, both sexes), were sourced from the Jackson Laboratory (stock#: 034840-JAX or 034848-JAX). Initially, these animals were group-housed in a climate-controlled vivarium under a reversed 12-h light/dark cycle (lights on at 7 PM), accredited by the Association for Assessment and Accreditation of Laboratory Animal Care. Upon initiation of experimental procedures, mice aged 4-9 months were individually housed and placed on a standard food-deprivation schedule, while maintaining free access to water, to achieve ~85% of their normal body weight. Seventeen 5XFAD and seventeen WT mice were allocated to undergo escalating predatory risk testing (Figure 1), while another set (5XFAD, n=11; WT, n=6) was subjected to combined tetrode recording and conditional predatory risk testing (Figure 2), as detailed below. All experiments were conducted during the dark phase in strict accordance with the guidelines of the University of Washington Institutional Animal Care and Use Committee (IACUC protocol #: 4040-01).

Surgery

Under isoflurane anesthesia, animals were secured in a stereotaxic instrument (Kopf) for microdrive array implantation, which contained individually movable tetrodes targeting the right dHPC (AP: -1.8, ML: +1.7, DV: -1.3; four tetrodes) and mPFC (AP: +1.8, ML: +0.3, DV: -1.2; four tetrodes). The tetrodes were fabricated

from formvar-insulated nichrome wire (14 µm diameter; Kanthal) and gold-plated to a final impedance of 100-300 kΩ (measured at 1 kHz). The assembly was secured with dental cement and bone screws. A recovery period of at least one week preceded the initiation of behavioral experiments and recording sessions.

Escalating predatory risk

This task utilized a custom-built apparatus with a nest area (inner dimensions: 14 cm length × 45 cm width × 61 cm height; 2.2 lux luminance) and an adjacent foraging space (104 cm length × 45 cm width × 61 cm height; 5.0 lux luminance; 72-dB white noise), monitored by the ANY-maze system (Stoelting Co.) and a ceiling-mounted HD webcam (C910; Logitech) for video tracking at 30 fps (Figure 1A). The protocol comprised ‘habituation,’ ‘baseline foraging,’ and ‘weasel predator testing’ phases.

During habituation, hunger-motivated mice were acclimated by being placed in the nest with 20 food pellets (45 mg, F0165, Bio-Serv) for 30 min/day over two days. For baseline foraging, mice received two 45-mg pellets in the nest. After eating these, they could access the foraging area, via an opened gateway, to retrieve pellets at 12.7 cm, 25.4 cm, and 38.1 cm distances from the nest, with three daily trials for four days.

Predator testing began with animals foraging for a pellet placed 38.1 cm from the nest across three trials. Subsequent trials introduced a taxidermy weasel on a wheeled frame at the foraging space's opposite end. As the mouse approached the pellet within ~12.7 cm, the weasel surged 30.4 cm towards the pellet at 60 cm/s via a pneumatic actuator, then returned to its starting position. Trials concluded either when the mouse secured the pellet or after 3 minutes, with the process repeated for pellets placed at

25.2 cm and 12.7 cm.

Conditional predatory task

Adapted from a figure-eight maze [39], this T-maze setup features a nest area at the base (dimensions: 92 cm length × 92 cm width × 79 cm height; 7 lux luminance) and two lateral goal arms, each concealed with a puppet eagle predator near a designated pellet zone (Figure 2A). Movement was tracked using headstage-mounted LEDs, integrated with ANY-maze (Stoelting Co.) and Cheetah (NeuraLynx, Inc.) systems. Importantly, this maze design ensured consistent location visits for optimal neural activity analysis.

The protocol comprised four phases: ‘habituation,’ ‘shaping,’ ‘baseline foraging,’ and ‘predator testing,’ with tetrodes adjusted towards the target areas as detailed in the ‘Unit recording and analyses’ section. During the two days of habituation, animals were placed in the nest for 30 min/day with ten grain (45 mg, F0165, Bio-Serv) and ten chocolate (45 mg, F0299, Bio-Serv) pellets for acclimation. In the shaping phase, mice received one grain and one chocolate pellet in the nest. Post-consumption, the nest gate opened, guiding them to a pellet at increasing distances. Each arm was consistently assigned a specific pellet type. After a forced arm pellet retrieval and consumption, the next trial started on the opposite arm. This phase lasted three days. During baseline foraging, with two nest pellets available, the gateway opened post-consumption, allowing free choice between left or right arm pellets. Choosing a pellet closed the opposite arm gate, with 6 trials/day for 8.6 ± 1.03 days. Predator testing sessions, during which neural recordings were

conducted, included pre-predator (8-14 trials), predator (3-10 trials), and post-predator (10 min in nest) phases. During predator trials, the puppet eagle surged forward (15.2 cm at a speed of 38 cm/s, via a linear actuator), when mice approached the preferred pellet. The predator remained hidden behind a black plastic block on the non-preferred pellet side. Pellet preference was measured using a Preference Index (PI), the ratio of preferred pellet procurement to total choices.

Contextual fear conditioning

After completing the conditional predatory risk task, 5XFAD and WT mice were placed in a standard operant chamber with a grid floor (stainless steel rods; 5 mm diameter, spaced 1 cm apart) [43]. Following a 3-minute baseline period, three unsignaled footshocks (0.7 mA, 1 sec) were administered 1 minute apart. Postshock freezing was assessed between shocks. The next day, the mice were returned to the same chamber, and their conditioned freezing response to the context was measured for 3 minutes before administering another set of 3 unsignaled shocks and assessing postshock freezing. An uninformed observer used a custom-written computer-assisted scoring program (in C language) to manually record the duration of freezing behavior in animals via keystrokes on a computer keyboard [44]. Freezing was defined as the absence of any visible movement in the body and vibrissae, except for respiratory movements [45]. The program applied a 2-second or more continuous inactivity threshold to identify freezing. The percentage of freezing was calculated by dividing the total duration of freezing by the total observation time and multiplying by 100.

Electrophysiological recording and analysis

Single-unit and local field potential (LFP) signals were amplified (10,000X), filtered (unit: 600 Hz to 6000 Hz; LFPs: 0.1 Hz to 1000 Hz), and digitized (32 kHz) using the Cheetah data acquisition system (Neuralynx). Unit isolation involved an automatic spike-sorting program (SpikeSort 3D; Neuralynx) and additional manual cutting, following protocols described in previous studies [17,18]. Raster plots and peristimulus time histograms were generated using NeuroExplorer (Nex Technologies).

Place cells were evaluated based on criteria established in prior research [18,40,41]. Specifically, units were selected if they exhibited stable, well-discriminated complex spike waveforms, a refractory period of at least 1 ms, peak firing rates > 2 Hz in any session, and spatial information > 0.5 bits/s in any session. Cells were categorized based on the peak positions of their place fields during the pre-predator session into nest cells (maximal firing in the nest), center cells (maximal firing in the center zone), risky arm cells (maximal firing in the maze arm close to the threat), and safe arm cells (maximal firing in the maze arm away from the threat). A pixel-by-pixel spatial correlation analysis was conducted using a customized R program to calculate the similarity of place maps between the pre-predator and predator sessions for each place cell. The correlation value (*r*) was transformed into a Fisher Z' score for parametric comparisons between cell types. Additionally, the program calculated the distance between each cell's peak firing locations across sessions, identifying the maximal firing locations (x and y coordinates in the maze) for each session and calculating the distance (in cm) between these points for the pre-predator versus predator sessions.

Cross-correlograms (CCs) of simultaneously recorded dHPC and mPFC units were generated using NeuroExplorer, following established methods [17,41]. CCs were constructed with dHPC cells as the reference, employing a 10-ms bin width for two time epochs: *pre-turn* (a 3-s epoch before the animal turned at the end of the center zone toward one of the arms during the pre-predator session) and *predator-turn* (a 3-s epoch before the turn during the predator session). To avoid false correlations due to covariation or nonstationary firing rates between the dHPC and mPFC, a 'Shift-Predictor' correction was applied, with trial shuffles performed 100 times (cf. [42]). Each shift predictor correlogram was subtracted from its respective raw correlogram, and Z-scores were calculated using the mean and standard deviation of the corrected CCs. A neural pair was deemed significantly correlated if the peak Z-score exceeded 3. Additional criteria required that the dHPC and mPFC firing rates during the pre-turn periods for both the pre-predator and predator sessions be above 0.2 Hz, and the peak of the CC had to fall within a ±100 ms testing window relative to the reference spikes.

LFP signals from a single channel of each animal's dHPC electrodes were band-pass filtered between 150 and 250 Hz using a zero-phase digital filter to minimize phase distortions. The envelope of these high-frequency oscillations was extracted using the Hilbert transform, providing a precise measure of their amplitude. The resulting envelope was then smoothed with a Gaussian-weighted moving average over a 40 ms window. SWR events were detected when the smoothed envelope exceeded a threshold of 4 standard deviations above the mean amplitude. The event ended when the amplitude fell below 2 standard deviations, ensuring precise delineation of event boundaries. We included only SWR events with durations over 15 milliseconds in the

analysis. All analyses were conducted using MATLAB 2024 Signal Processing Toolbox, which provided the necessary tools for detailed signal examination and processing. To assess the modulatory effects of SWRs on dHPC and mPFC unit activities, unit firing rates were normalized to the pre-SWR baseline periods (dHPC: -500 to -250 ms; mPFC: -1000 to -500 ms). A neuron was considered significantly activated if its peak Z-score exceeded 3 within a specified time window around SWR onset (dHPC: ±100 ms or ±250 ms; mPFC: ±250-ms or ±500 ms).

Statistical analyses

Statistical significance was evaluated using several tests, including One-way repeated measured ANOVA, two-way ANOVA, linear regression, unpaired *t*-test, Kruskal-Wallis test, Friedman test, and Mann-Whitney *U* test. These tests were chosen to accommodate the diverse data structures encountered in our study. Post hoc analyses, when necessary, were conducted using Bonferroni or Wilcoxon signed rank tests. The choice between parametric and nonparametric tests was guided by the Kolmogorov-Smirnov normality test, ensuring the appropriate statistical approach was applied on the data distribution. Detailed statistical information for each analysis is provided in the legends of each figure. Statistical significance was established at a threshold of $p < 0.05$. Statistical analyses and graph generation were performed using SPSS (ver. 19), custom MATLAB codes, GraphPad Prism (ver. 9.00), and NeuroExplorer (ver. 5.030).

Histology

After concluding the experiment, electrolytic lesions were created by applying currents (10 µA, 10 s) to the tetrode tips to mark electrode placements. Mice were then euthanized with an overdose of Beuthanasia and perfused intracardially with phosphate-buffered saline (PBS), followed by fixation with 4% paraformaldehyde in PBS. The brains were extracted and stored overnight in the fixative at 4 °C. Subsequently, they were kept in sucrose solutions of increasing concentrations (10%, 20%, and 30%), remaining in each solution until they sank to the bottom. For Aβ immunostaining, transverse sections (30 µm) were rinsed in PBS and incubated for 1 hr in 5% normal goat serum with 0.5% TritonX in PBS to block non-specific binding. This step was followed by overnight incubation at 4 °C with Aβ-specific mouse monoclonal antibody (1:1000, Medimabs, McSA1). After thorough washing, the sections were incubated with a goat anti-mouse secondary antibody conjugated to Alexa Fluor 568 (1:250, Abcam, ab175473) for 2 hr at room temperature. Prepared sections were then mounted on slides and cover slipped with Flouromount-G™ containing DAPI (eBioscience) for nuclear staining, facilitating imaging with a Keyence BZ-X800E microscope. Image analysis was performed using ImageJ software (NIH, version 1.54d). A separate set of sections was mounted onto gelatinized slides and stained with Cresyl violet and Prussian blue to confirm the precise locations of the tetrode tips.

ACKNOWLEGMENTS

This study was supported by the National Institutes of Health grants AG067008 (E.J.K.), MH099073 (J.J.K.), the University of Washington Royalty Research Fund A188443 (E.J.K.), and the Ministry of Science and ICT through the National Research Foundation of Korea grant: Brain Science Research Program NRF-2022M3E5E8018421 and NRF-2022R1A2C2009265 (J.C.). We thank Drs. Min Whan Jung and Jong Won Lee from the Korea Advanced Institute of Science and Technology for generously sharing their custom-made microdrive parts and electronic interface boards, and Nayoung Kim for her assistance with experiments and data collection/analysis. Cartoons in Figures 1A, 2B, 2H, 3C, 4A, 4F, 4J, S1A, and S5B were created with BioRender.com

AUTHOR CONTRIBUTIONS

E.J.K., J.C., and J.J.K. designed research; E.J.K., S.G.P., B.P.S., and H.B. performed behavioral and neurophysiological experiments and analyses; and E.J.K., S.G.P., J.C., and J.J.K. wrote the manuscript.

DECLARATION OF INTERESTS

The authors declare no competing interests.

DATA AVAILABILITY

The datasets and analysis code of this research will be made available in the Dryad data repository (https://datadryad.org/stash/dataset/doi:10.5061/dryad.51c59zwgk) upon acceptance of the manuscript.

REFERENCES

1. Gleichgerrcht E, Ibanez A, Roca M, Torralva T, Manes F. Decision-making cognition in neurodegenerative diseases. *Nat Rev Neurol*. 2010;6:611-623. doi:10.1038/nrneurol.2010.148
2. Toepper M. Dissociating Normal Aging from Alzheimer's Disease: A View from Cognitive Neuroscience. *J Alzheimers Dis*. 2017;57:331-352. doi:10.3233/JAD-161099
3. Fernandes C, Macedo I, Barbosa F, Marques-Teixeira J. Economic decision-making in the continuum between healthy aging and Alzheimer's Disease: A systematic review of 20 years of research. *Neurosci Biobehav Rev*. 2021;131:1243-1263. doi:10.1016/j.neubiorev.2021.10.030
4. Gaubert F, Chainay H. Decision-Making Competence in Patients with Alzheimer's Disease: A Review of the Literature. *Neuropsychol Rev*. 2021;31:267-287. doi:10.1007/s11065-020-09472-2
5. Ha J, Kim EJ, Lim S, et al. Altered risk-aversion and risk-taking behaviour in patients with Alzheimer's disease. *Psychogeriatrics*. 2012;12:151-158. doi:10.1111/j.1479-8301.2011.00396.x
6. Sinz H, Zamarian L, Benke T, Wenning GK, Delazer M. Impact of ambiguity and risk on decision making in mild Alzheimer's disease. *Neuropsychologia*. 2008;46:2043-2055. doi:10.1016/j.neuropsychologia.2008.02.002
7. Bayard S, Jacus JP, Raffard S, Gely-Nargeot MC. Apathy and emotion-based decision-making in amnesic mild cognitive impairment and Alzheimer's disease. *Behav Neurol*. 2014;2014:231469. doi:10.1155/2014/231469
8. Anderson R, Hart DW, Sweis B, et al. Sex-specific interactions between procedural and deliberative decision-making systems in a mouse model of Alzheimer’s disease. *bioRxiv*. 2021. doi:10.1101/2021.03.16.435712
9. Delazer M, Sinz H, Zamarian L, Benke T. Decision-making with explicit and stable rules in mild Alzheimer's disease. *Neuropsychologia*. 2007;45:1632-1641. doi:10.1016/j.neuropsychologia.2007.01.006
10. Corcoran KA, Maren S. Hippocampal inactivation disrupts contextual retrieval of fear memory after extinction. *J Neurosci*. 2001;21:1720-1726.
11. Corcoran KA, Quirk GJ. Activity in prelimbic cortex is necessary for the expression of learned, but not innate, fears. *J Neurosci*. 2007;27:840-844. doi:10.1523/JNEUROSCI.5327-06.2007
12. Gluth S, Sommer T, Rieskamp J, Buchel C. Effective Connectivity between Hippocampus and Ventromedial Prefrontal Cortex Controls Preferential Choices from Memory. *Neuron*. 2015;86:1078-1090. doi:10.1016/j.neuron.2015.04.023
13. Rhodes SE, Murray EA. Differential effects of amygdala, orbital prefrontal cortex, and prelimbic cortex lesions on goal-directed behavior in rhesus macaques. *J Neurosci*. 2013;33:3380-3389. doi:10.1523/JNEUROSCI.4374-12.2013
14. Yoon T, Okada J, Jung MW, Kim JJ. Prefrontal cortex and hippocampus subserve different components of working memory in rats. *Learn Mem*. 2008;15:97-105. doi:10.1101/lm.850808
15. Yu JY, Frank LM. Hippocampal-cortical interaction in decision making. *Neurobiol*

Learn Mem. 2015;117:34-41. doi:10.1016/j.nlm.2014.02.002
16. Euston DR, Gruber AJ, McNaughton BL. The role of medial prefrontal cortex in memory and decision making. *Neuron*. 2012;76:1057-1070. doi:10.1016/j.neuron.2012.12.002
17. Kim EJ, Kong MS, Park SG, Mizumori SJY, Cho J, Kim JJ. Dynamic coding of predatory information between the prelimbic cortex and lateral amygdala in foraging rats. *Sci Adv*. 2018;4:eaar7328. doi:10.1126/sciadv.aar7328
18. Kim EJ, Park M, Kong MS, Park SG, Cho J, Kim JJ. Alterations of hippocampal place cells in foraging rats facing a "predatory" threat. *Curr Biol*. 2015;25:1362-1367. doi:10.1016/j.cub.2015.03.048
19. Eimer WA, Vassar R. Neuron loss in the 5XFAD mouse model of Alzheimer's disease correlates with intraneuronal Abeta42 accumulation and Caspase-3 activation. *Mol Neurodegener*. 2013;8:2. doi:10.1186/1750-1326-8-2
20. Oakley H, Cole SL, Logan S, et al. Intraneuronal beta-amyloid aggregates, neurodegeneration, and neuron loss in transgenic mice with five familial Alzheimer's disease mutations: potential factors in amyloid plaque formation. *J Neurosci*. 2006;26:10129-10140. doi:10.1523/JNEUROSCI.1202-06.2006
21. Girard SD, Baranger K, Gauthier C, et al. Evidence for early cognitive impairment related to frontal cortex in the 5XFAD mouse model of Alzheimer's disease. *J Alzheimers Dis*. 2013;33:781-796. doi:10.3233/JAD-2012-120982
22. Sadleir KR, Popovic J, Vassar R. ER stress is not elevated in the 5XFAD mouse model of Alzheimer's disease. *J Biol Chem*. 2018;293:18434-18443. doi:10.1074/jbc.RA118.005769
23. Girardeau G, Inema I, Buzsaki G. Reactivations of emotional memory in the hippocampus-amygdala system during sleep. *Nat Neurosci*. 2017;20:1634-1642. doi:10.1038/nn.4637
24. Schmidt B, Redish AD. Disrupting the medial prefrontal cortex with designer receptors exclusively activated by designer drug alters hippocampal sharp-wave ripples and their associated cognitive processes. *Hippocampus*. 2021;31:1051-1067. doi:10.1002/hipo.23367
25. Colgin LL. Oscillations and hippocampal-prefrontal synchrony. *Curr Opin Neurobiol*. 2011;21:467-474. doi:10.1016/j.conb.2011.04.006
26. den Bakker H, Van Dijck M, Sun JJ, Kloosterman F. Sharp-wave-ripple-associated activity in the medial prefrontal cortex supports spatial rule switching. *Cell Rep*. 2023;42:112959. doi:10.1016/j.celrep.2023.112959
27. Jadhav SP, Rothschild G, Roumis DK, Frank LM. Coordinated Excitation and Inhibition of Prefrontal Ensembles during Awake Hippocampal Sharp-Wave Ripple Events. *Neuron*. 2016;90:113-127. doi:10.1016/j.neuron.2016.02.010
28. Jura B, Macrez N, Meyrand P, Bem T. Deficit in hippocampal ripples does not preclude spatial memory formation in APP/PS1 mice. *Sci Rep*. 2019;9:20129. doi:10.1038/s41598-019-56582-w
29. Iaccarino HF, Singer AC, Martorell AJ, et al. Gamma frequency entrainment attenuates amyloid load and modifies microglia. *Nature*. 2016;540:230-235. doi:10.1038/nature20587
30. Prince SM, Paulson AL, Jeong N, Zhang L, Amigues S, Singer AC. Alzheimer's

pathology causes impaired inhibitory connections and reactivation of spatial codes during spatial navigation. *Cell Rep*. 2021;35:109008. doi:10.1016/j.celrep.2021.109008
31. Gillespie AK, Jones EA, Lin YH, et al. Apolipoprotein E4 Causes Age-Dependent Disruption of Slow Gamma Oscillations during Hippocampal Sharp-Wave Ripples. *Neuron*. 2016;90:740-751. doi:10.1016/j.neuron.2016.04.009
32. Jones EA, Gillespie AK, Yoon SY, Frank LM, Huang Y. Early Hippocampal Sharp-Wave Ripple Deficits Predict Later Learning and Memory Impairments in an Alzheimer's Disease Mouse Model. *Cell Rep*. 2019;29:2123-2133 e2124. doi:10.1016/j.celrep.2019.10.056
33. Krakauer JW, Ghazanfar AA, Gomez-Marin A, MacIver MA, Poeppel D. Neuroscience Needs Behavior: Correcting a Reductionist Bias. *Neuron*. 2017;93:480-490. doi:10.1016/j.neuron.2016.12.041
34. Kempermann G, Kuhn HG, Gage FH. More hippocampal neurons in adult mice living in an enriched environment. *Nature*. 1997;386:493-495. doi:10.1038/386493a0
35. Bennett EL, Diamond MC, Krech D, Rosenzweig MR. Chemical and Anatomical Plasticity Brain. *Science*. 1964;146:610-619. doi:10.1126/science.146.3644.610
36. Pellman BA, Kim JJ. What Can Ethobehavioral Studies Tell Us about the Brain's Fear System? *Trends Neurosci*. 2016;39:420-431. doi:10.1016/j.tins.2016.04.001
37. Choi JS, Kim JJ. Amygdala regulates risk of predation in rats foraging in a dynamic fear environment. *Proc Natl Acad Sci U S A*. 2010;107:21773-21777. doi:10.1073/pnas.1010079108
38. Kim JJ, Choi J-S, Lee HJ. Foraging in the face of fear: novel strategies for evaluating amygdala functions in rats. In: Amaral DG, Adolphs R, eds. Living Without an Amygdala. New York: The Guilford Press; 2016.
39. Pedigo SF, Song EY, Jung MW, Kim JJ. A computer vision-based automated Figure-8 maze for working memory test in rodents. *J Neurosci Methods*. 2006;156:10-16. doi:10.1016/j.jneumeth.2006.01.029
40. Grieves RM, Jedidi-Ayoub S, Mishchanchuk K, Liu A, Renaudineau S, Jeffery KJ. The place-cell representation of volumetric space in rats. *Nat Commun*. 2020;11:789. doi:10.1038/s41467-020-14611-7
41. Kong MS, Kim EJ, Park S, et al. 'Fearful-place' coding in the amygdala-hippocampal network. *Elife*. 2021;10. doi:10.7554/eLife.72040
42. Burgos-Robles A, Kimchi EY, Izadmehr EM, et al. Amygdala inputs to prefrontal cortex guide behavior amid conflicting cues of reward and punishment. *Nat Neurosci*. 2017;20:824-835. doi:10.1038/nn.4553
43. Chen C, Kim JJ, Thompson RF, Tonegawa S. Hippocampal lesions impair contextual fear conditioning in two strains of mice. *Behav Neurosci*. 1996;110:1177-1180.
44. Kim EJ, Kim ES, Covey E, Kim JJ. Social transmission of fear in rats: the role of 22-kHz ultrasonic distress vocalization. *PLoS One*. 2010;5:e15077. doi:10.1371/journal.pone.0015077
45. Blanchard RJ, Blanchard DC. Crouching as an index of fear. *J Comp Physiol Psychol*. 1969;67:370-375. doi:10.1037/h0026779

46. Gorrie CA, Brown J, Waite PM. Crash characteristics of older pedestrian fatalities: dementia pathology may be related to 'at risk' traffic situations. *Accid Anal Prev*. 2008;40:912-919. doi:10.1016/j.aap.2007.10.006
47. Sun T, Xie T, Wang J, et al. Decision-Making Under Ambiguity or Risk in Individuals With Alzheimer's Disease and Mild Cognitive Impairment. *Front Psychiatry*. 2020;11:218. doi:10.3389/fpsyt.2020.00218
48. Buzsaki G. Hippocampal sharp wave-ripple: A cognitive biomarker for episodic memory and planning. *Hippocampus*. 2015;25:1073-1188. doi:10.1002/hipo.22488
49. Joo HR, Frank LM. The hippocampal sharp wave-ripple in memory retrieval for immediate use and consolidation. *Nat Rev Neurosci*. 2018;19:744-757. doi:10.1038/s41583-018-0077-1
50. Norman Y, Yeagle EM, Khuvis S, Harel M, Mehta AD, Malach R. Hippocampal sharp-wave ripples linked to visual episodic recollection in humans. *Science*. 2019;365. doi:10.1126/science.aax1030
51. Fernandez-Ruiz A, Oliva A, Fermino de Oliveira E, Rocha-Almeida F, Tingley D, Buzsaki G. Long-duration hippocampal sharp wave ripples improve memory. *Science*. 2019;364:1082-1086. doi:10.1126/science.aax0758
52. Cowen SL, Gray DT, Wiegand JL, Schimanski LA, Barnes CA. Age-associated changes in waking hippocampal sharp-wave ripples. *Hippocampus*. 2020;30:28-38. doi:10.1002/hipo.23005
53. Wiegand JP, Gray DT, Schimanski LA, Lipa P, Barnes CA, Cowen SL. Age Is Associated with Reduced Sharp-Wave Ripple Frequency and Altered Patterns of Neuronal Variability. *J Neurosci*. 2016;36:5650-5660. doi:10.1523/JNEUROSCI.3069-15.2016
54. Papale AE, Zielinski MC, Frank LM, Jadhav SP, Redish AD. Interplay between Hippocampal Sharp-Wave-Ripple Events and Vicarious Trial and Error Behaviors in Decision Making. *Neuron*. 2016;92:975-982. doi:10.1016/j.neuron.2016.10.028
55. Jarovi J, Pilkiw M, Takehara-Nishiuchi K. Prefrontal neuronal ensembles link prior knowledge with novel actions during flexible action selection. *Cell Rep*. 2023;42:113492. doi:10.1016/j.celrep.2023.113492
56. Tang W, Shin JD, Frank LM, Jadhav SP. Hippocampal-Prefrontal Reactivation during Learning Is Stronger in Awake Compared with Sleep States. *J Neurosci*. 2017;37:11789-11805. doi:10.1523/JNEUROSCI.2291-17.2017
57. Morris JK, Vidoni ED, Johnson DK, et al. Aerobic exercise for Alzheimer's disease: A randomized controlled pilot trial. *PLoS One*. 2017;12:e0170547. doi:10.1371/journal.pone.0170547
58. Scarmeas N, Stern Y, Tang MX, Mayeux R, Luchsinger JA. Mediterranean diet and risk for Alzheimer's disease. *Ann Neurol*. 2006;59:912-921. doi:10.1002/ana.20854
59. Mangialasche F, Solomon A, Winblad B, Mecocci P, Kivipelto M. Alzheimer's disease: clinical trials and drug development. *Lancet Neurol*. 2010;9:702-716. doi:10.1016/S1474-4422(10)70119-8
60. Tuszynski MH, Thal L, Pay M, et al. A phase 1 clinical trial of nerve growth factor gene therapy for Alzheimer disease. *Nat Med*. 2005;11:551-555. doi:10.1038/nm1239
61. Pople CB, Meng Y, Li DZ, et al. Neuromodulation in the Treatment of Alzheimer's

Disease: Current and Emerging Approaches. *J Alzheimers Dis*. 2020;78:1299-1313. doi:10.3233/JAD-200913
62. Vogt NM, Kerby RL, Dill-McFarland KA, et al. Gut microbiome alterations in Alzheimer's disease. *Sci Rep*. 2017;7:13537. doi:10.1038/s41598-017-13601-y
63. Cacucci F, Yi M, Wills TJ, Chapman P, O'Keefe J. Place cell firing correlates with memory deficits and amyloid plaque burden in Tg2576 Alzheimer mouse model. *Proc Natl Acad Sci U S A*. 2008;105:7863-7868. doi:10.1073/pnas.0802908105
64. Zhang H, Chen L, Johnston KG, et al. Degenerate mapping of environmental location presages deficits in object-location encoding and memory in the 5xFAD mouse model for Alzheimer's disease. *Neurobiol Dis*. 2023;176:105939. doi:10.1016/j.nbd.2022.105939
65. Mably AJ, Gereke BJ, Jones DT, Colgin LL. Impairments in spatial representations and rhythmic coordination of place cells in the 3xTg mouse model of Alzheimer's disease. *Hippocampus*. 2017;27:378-392. doi:10.1002/hipo.22697
66. Jun H, Bramian A, Soma S, Saito T, Saido TC, Igarashi KM. Disrupted Place Cell Remapping and Impaired Grid Cells in a Knockin Model of Alzheimer's Disease. *Neuron*. 2020;107:1095-1112 e1096. doi:10.1016/j.neuron.2020.06.023
67. Ying J, Keinath AT, Lavoie R, Vigneault E, El Mestikawy S, Brandon MP. Disruption of the grid cell network in a mouse model of early Alzheimer's disease. *Nat Commun*. 2022;13:886. doi:10.1038/s41467-022-28551-x
68. Cayzac S, Mons N, Ginguay A, Allinquant B, Jeantet Y, Cho YH. Altered hippocampal information coding and network synchrony in APP-PS1 mice. *Neurobiol Aging*. 2015;36:3200-3213. doi:10.1016/j.neurobiolaging.2015.08.023
69. Elder GA, Gama Sosa MA, De Gasperi R. Transgenic mouse models of Alzheimer's disease. *Mt Sinai J Med*. 2010;77:69-81. doi:10.1002/msj.20159
70. Gotz J, Ittner LM. Animal models of Alzheimer's disease and frontotemporal dementia. *Nat Rev Neurosci*. 2008;9:532-544. doi:10.1038/nrn2420
71. Jankowsky JL, Zheng H. Practical considerations for choosing a mouse model of Alzheimer's disease. *Mol Neurodegener*. 2017;12:89. doi:10.1186/s13024-017-0231-7
72. Kim JJ, Fanselow MS. Modality-specific retrograde amnesia of fear. *Science*. 1992;256:675-677. doi:10.1126/science.1585183
73. Phillips RG, LeDoux JE. Differential contribution of amygdala and hippocampus to cued and contextual fear conditioning. *Behav Neurosci*. 1992;106:274-285. doi:10.1037//0735-7044.106.2.274
74. Kimura R, Ohno M. Impairments in remote memory stabilization precede hippocampal synaptic and cognitive failures in 5XFAD Alzheimer mouse model. *Neurobiol Dis*. 2009;33:229-235. doi:10.1016/j.nbd.2008.10.006

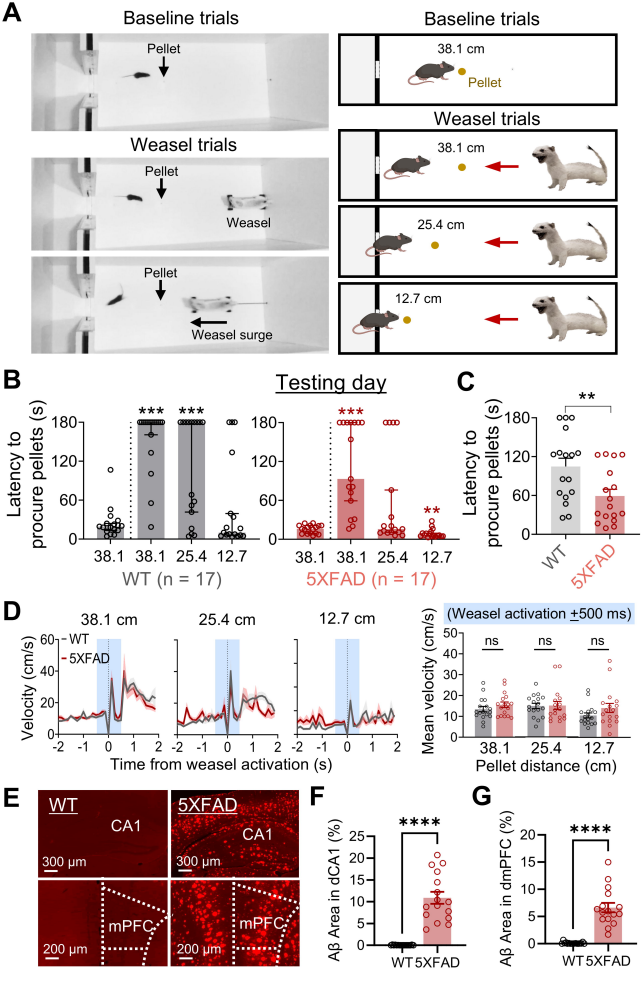
A
Baseline trials
Pellet
Weasel trials
Pellet
Weasel
Pellet
Weasel surge
Baseline trials
38.1 cm
Pellet
Weasel trials
38.1 cm
25.4 cm
12.7 cm
B
Testing day
Latency to procure pellets (s)
***
***
***
**
38.1
38.1
25.4
12.7
WT (n = 17)
5XFAD (n = 17)
C
Latency to procure pellets (s)
**
WT
5XFAD
D
38.1 cm
25.4 cm
12.7 cm
WT
5XFAD
Velocity (cm/s)
Time from weasel activation (s)
(Weasel activation ±500 ms)
Mean velocity (cm/s)
ns
ns
ns
38.1
25.4
12.7
Pellet distance (cm)
E
WT
CA1
300 µm
5XFAD
CA1
300 µm
mPFC
200 µm
mPFC
200 µm
F
Aβ Area in dCA1 (%)
****
WT
5XFAD
G
Aβ Area in dmPFC (%)
****
WT
5XFAD

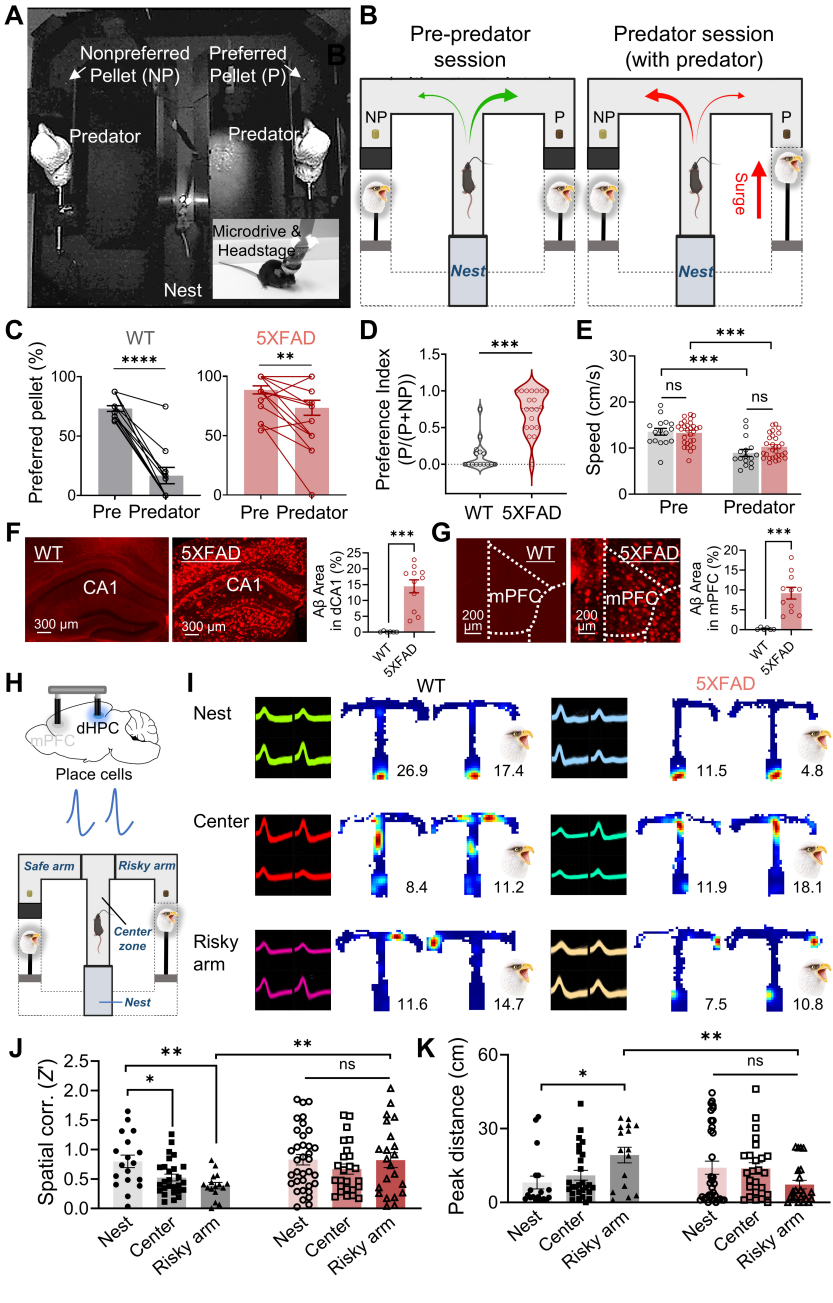
A
Nonpreferred Pellet (NP)
Preferred Pellet (P)
Predator
Predator
Microdrive & Headstage
Nest
B
Pre-predator session
Predator session (with predator)
NP
P
Nest
Surge
C
WT
5XFAD
Preferred pellet (%)
Pre
Predator
D
Preference Index (P/(P+NP))
WT
5XFAD
E
Speed (cm/s)
ns
Pre
Predator
F
WT
5XFAD
CA1
300 µm
Aβ Area in dCA1 (%)
G
mPFC
200 µm
Aβ Area in mPFC (%)
H
dHPC
mPFC
Place cells
Safe arm
Risky arm
Center zone
Nest
I
WT
5XFAD
Nest
Center
Risky arm
26.9
17.4
11.5
4.8
8.4
11.2
11.9
18.1
11.6
14.7
7.5
10.8
J
Spatial corr. (Z)
Nest
Center
Risky arm
K
Peak distance (cm)

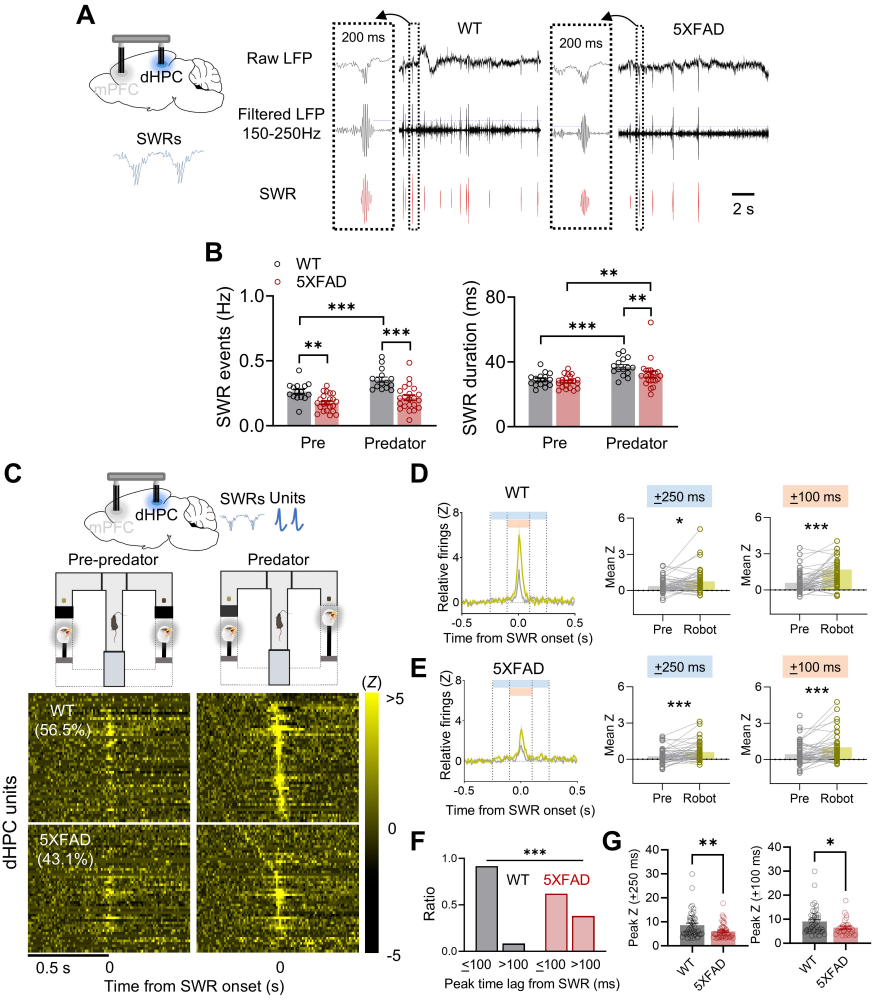
A
dHPC
mPFC
SWRs
Raw LFP
Filtered LFP
150-250Hz
SWR
200 ms
WT
5XFAD
2 s
B
WT
5XFAD
SWR events (Hz)
SWR duration (ms)
Pre
Predator
C
SWRs Units
Pre-predator
Predator
WT
(56.5%)
5XFAD
(43.1%)
dHPC units
(Z)
>5
0
-5
0.5 s
Time from SWR onset (s)
D
WT
Relative firings (Z)
Time from SWR onset (s)
±250 ms
±100 ms
Mean Z
Pre
Robot
E
5XFAD
F
Ratio
≤100
>100
Peak time lag from SWR (ms)
G
Peak Z (±250 ms)
Peak Z (±100 ms)

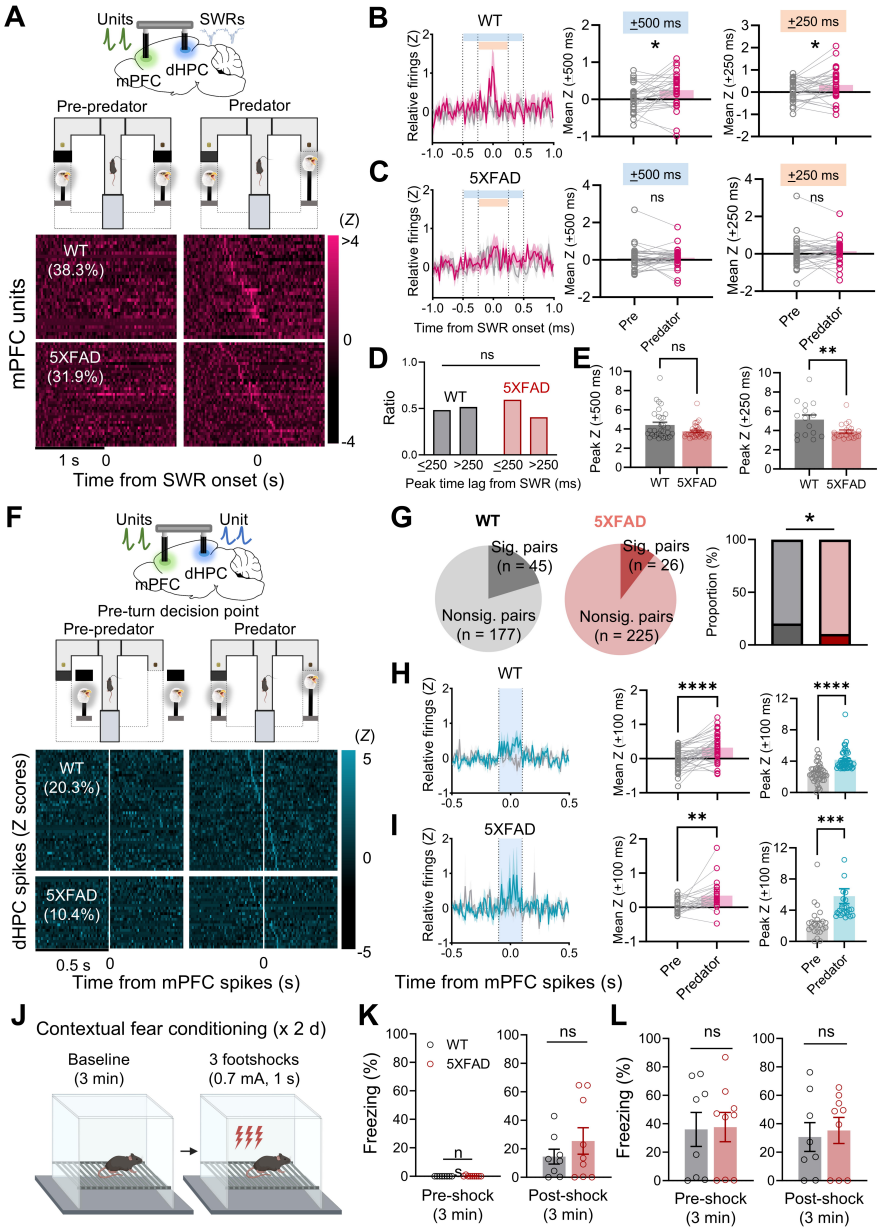
A
Units
SWRs
mPFC
dHPC
Pre-predator
Predator
mPFC units
WT
(38.3%)
5XFAD
(31.9%)
(Z)
>4
0
-4
1 s
0
0
Time from SWR onset (s)
B
WT
Relative firings (Z)
±500 ms
±250 ms
Mean Z (+500 ms)
Mean Z (+250 ms)
*
*
C
5XFAD
ns
ns
Time from SWR onset (ms)
Pre
Predator
D
ns
Ratio
WT
5XFAD
≤250
>250
≤250
>250
Peak time lag from SWR (ms)
E
ns
**
Peak Z (+500 ms)
Peak Z (+250 ms)
WT
5XFAD
F
Units
Unit
mPFC
dHPC
Pre-turn decision point
Pre-predator
Predator
dHPC spikes (Z scores)
WT
(20.3%)
5XFAD
(10.4%)
(Z)
5
0
-5
0.5 s
0
0
Time from mPFC spikes (s)
G
WT
Sig. pairs
(n = 45)
Nonsig. pairs
(n = 177)
5XFAD
Sig. pairs
(n = 26)
Nonsig. pairs
(n = 225)
*
Proportion (%)
H
WT
Relative firings (Z)
****
****
Mean Z (+100 ms)
Peak Z (+100 ms)
I
5XFAD
**
***
Time from mPFC spikes (s)
Pre
Predator
J
Contextual fear conditioning (x 2 d)
Baseline
(3 min)
3 footshocks
(0.7 mA, 1 s)
K
WT
5XFAD
Freezing (%)
n
ns
Pre-shock
(3 min)
Post-shock
(3 min)
L
ns
ns
Freezing (%)
Pre-shock
(3 min)
Post-shock
(3 min)